HHS Public Access

Author manuscript

Radiat Res. Author manuscript; available in PMC 2018 September 01.

Published in final edited form as:

Radiat Res. 2017 September ; 188(3): 303–313. doi:10.1667/RR14662.1.

Identifying Voxels at Risk for Progression in Glioblastoma Based on Dosimetry, Physiologic and Metabolic MRI

Mekhail Anwar[a,1], **Annette M. Molinaro**[b], **Olivier Morin**[a], **Susan M. Chang**[c], **Daphne A. Haas-Kogan**[a], **Sarah J. Nelson**[d], and **Janine M. Lupo**[d]

[a]Department of Radiation Oncology, University of California, San Francisco, California

[b]Department of Neurosurgery, Division of Epidemiology and Biostatistics, University of California, San Francisco, California

[c]Department of Neurosurgery, Division of Neuro-oncology, University of California, San Francisco, California

[d]Department of Radiology and Biomedical Imaging, University of California, San Francisco, California

Abstract

Despite the longstanding role of radiation in cancer treatment and the presence of advanced, high-resolution imaging techniques, delineation of voxels at-risk for progression remains purely a geometric expansion of anatomic images, missing subclinical disease at risk for recurrence while treating potentially uninvolved tissue and increasing toxicity. This remains despite the modern ability to precisely shape radiation fields. A striking example of this is the treatment of glioblastoma, a highly infiltrative tumor that may benefit from accurate identification of subclinical disease. In this study, we hypothesize that parameters from physiologic and metabolic magnetic resonance imaging (MRI) at diagnosis could predict the likelihood of voxel progression at radiographic recurrence in glioblastoma by identifying voxel characteristics that indicate subclinical disease. Integrating dosimetry can reveal its effect on voxel outcome, enabling risk-adapted voxel dosing. As a system example, 24 patients with glioblastoma treated with radiotherapy, temozolomide and an anti-angiogenic agent were analyzed. Pretreatment median apparent diffusion coefficient (ADC), fractional anisotropy (FA), relative cerebral blood volume (rCBV), vessel leakage (percentage recovery), cho-line-to-NAA index (CNI) and dose of voxels in the T2 nonenhancing lesion (NEL), T1 post-contrast enhancing lesion (CEL) or normal-appearing volume (NAV) of brain, were calculated for voxels that progressed [NAV→NEL, CEL (N = 8,765)] and compared against those that remained stable [NAV→NAV (N = 98,665)]. Voxels that progressed (NAV→NEL) had significantly different ($P < 0.01$) ADC (860), FA (0.36) and CNI (0.67) versus stable voxels (804, 0.43 and 0.05, respectively), indicating increased cell turnover, edema and decreased directionality, consistent with subclinical disease. NAV→CEL voxels were more abnormal (1,014, 0.28, 2.67, respectively) and leakier (percentage recovery = 70). A predictive model identified areas of recurrence, demonstrating that elevated CNI potentiates abnormal diffusion, even far (>2 cm) from the tumor and dose escalation >45 Gy has diminishing

[1]Address for correspondence: Radiation Oncology, University of California, San Francisco, 1825 4th Street, M2260, San Francisco, CA 94158; anwarme@radonc.ucsf.edu.

benefits. Integrating advanced MRI with dosimetry can identify at voxels at risk for progression and may allow voxel-level risk-adapted dose escalation to subclinical disease while sparing normal tissue. When combined with modern planning software, this technique may enable risk-adapted radiotherapy in any disease site with multimodal imaging.

INTRODUCTION

Despite both advances in modern imaging and the ability to precisely deliver radiation in highly complex spatial distributions, defining tissue at risk for progression for radiation planning remains largely an empiric geometric expansion of gross tumor visualized on anatomic imaging sequences. This has the unintended consequences of missing subclinically involved tissue, adversely affecting clinical outcomes, as well as irradiating normal tissue, thereby increasing toxicity. While applicable to a wide array of cancers, this paradigm is particularly relevant to the treatment of glioblastoma, which despite advancements in both technology and therapeutics over the last several decades, remains one of the most aggressive brain tumors, with a median survival of only 12–15 months (1). This poor outcome is mainly due to the difficulty of defining and treating the full extent of this highly infiltrative (2) tumor while sparing uninvolved brain. Although advanced imaging and surgical techniques combined with radiation and chemotherapy have improved outcome (3–5) with more conformal radiotherapy techniques (6) having enhanced the ability to deliver targeted radiation, recurrences remain largely local with 90% occurring within 2 cm of the original tumor (7, 8). To further complicate matters, the advent of anti-angiogenic agents, both in the upfront (9, 10) and recurrent settings (11), is changing the pattern of recurrence, with tumor often recurring as a nonenhancing, diffusely invasive phenotype (12). Despite these factors, current treatment planning guidelines for high-grade gliomas still do not take into account any magnetic resonance (MR) imaging beyond conventional post-contrast T1-weighted and T2-weighted FLAIR sequences when prescribing the cumulative radiation dose to be delivered. An improved method of risk-adapted radiotherapy based on a voxel's likelihood of progression is becoming imperative.

Significant recent advances in physiologic and metabolic imaging using MR (13, 14) enable voxel-level characterization of the brain parenchyma beyond the traditional anatomic T1 and T2 sequences, allowing visualization of cellular-level parameters that are indicative of tumor involvement. Subclinical invasion results in increased edema and decreased directionality along white matter tracts reflected by an increased apparent diffusion coefficient (ADC) and decreased fractional anisotropy (FA), respectively. Dynamic susceptibility contrast (DSC) perfusion-weighted imaging (PWI) facilitates assessment of the vasculature in terms of the amount or size of blood vessels (relative cerebral blood volume or rCBV) and leakiness (percentage recovery) that is typical of the poor tumor neovasculature and reflected by an increase in rCBV and decrease in percentage recovery, respectively. ^{1}H magnetic resonance spectroscopic imaging (MRSI), specifically using the choline-to-NAA index (CNI), allows visualization of cellular turnover associated with tumor growth. The combination of these techniques provides more detailed information regarding tumor burden (15, 16) and malignant behavior, and has been closely associated with both progression-free (17) and overall survival (18). While the use of these parameters can aid in identifying voxels that are

likely to progress and facilitate the delineation of at-risk areas for radiation treatment planning, there is currently no method for integrating voxel-level metabolic and physiologic characteristics with dosimetry to guide clinicians in prescribing the optimal dose per voxel.

The goal of this study was to demonstrate a technique for integrating dosimetry and multiparametric imaging that consisted of pre-radiotherapy metabolic and physiologic MRI to both identify voxels at risk for progression and create a model for risk-adapted radiotherapy planning. This report hypothesizes that there would be anatomically normal-appearing voxels that harbor subclinical disease and would therefore have physiologic and metabolic characteristics more similar to abnormal voxels. To identify anatomically normal-appearing voxels at risk for progression, we integrated spectroscopic, diffusion- and perfusion-weighted MRI parameters with dosimetry to detect voxel-level subclinical disease at diagnosis and predict the likelihood of voxel progression at radiographic recurrence. Incorporating dosimetry can also reveal its effect on voxel outcome, enabling risk-adapted voxel dosing.

MATERIALS AND METHODS

Patient Population

A total of 24 patients with newly diagnosed primary glioblastoma, whose radiation dosimetry maps were available, were retrospectively examined in this study. All patients had undergone surgical resection and subsequently participated in one of two clinical trials that consisted of treatment with a standard six-week cycle of external beam radiation and concurrent and adjuvant chemotherapy with temozolomide [75 mg/m^2 daily during radiotherapy and 200 mg/m^2 for five days every 28-day cycle after radiotherapy based on the Stupp regimen (5)] plus agents that have anti-angiogenic properties. Eleven patients were treated with enzastaurin (250 mg daily) (19, 20), while 13 patients received erlotinib (150 mg/day continuously or 500 mg/ day continuously if on anti-epileptic drugs starting on day 1 of radiotherapy) and bevacizumab (10 mg/kg every 14 days starting in week 2 of radiotherapy). Patient ranged from 25 to 70 years of age, with a median of 52 years old. To be included in the study, patients had to have a Karnofsky performance score of at least 60, while those who discontinued therapy because of adverse effects were excluded. All patients provided informed consent in accordance with guidelines established by our Institutional Review Board.

Patients had baseline (after surgical resection, before radio- and chemotherapy) imaging that included diffusion-weighted imaging (DWI), DSC-PWI and MRSI. One patient did not have PWI at the baseline scan. Patients received follow-up imaging examinations approximately every two months. Radiographic progression was defined by an experienced neuroradiologist in concurrence with a multi-interdisciplinary tumor board. To address the potential for pseudoprogression, the clinical histories of patients who either progressed within 12 weeks of the completion of radiotherapy or had a suspect scan followed by stable disease were centrally re-reviewed by a neuro-oncologist. If reoperation was performed, true progression in the location of recurrence was confirmed according to the recommendations of Wen *et al.* (21). Based on these criteria, none of the patients in this study exhibited pseudoprogression.

MR Image Acquisition

All MR data were acquired on a 3T GE scanner (GE Healthcare, Waukesha, WI) with an 8-channel head coil. Anatomic MR imaging included axial T2-weighted fluid attenuated inversion recovery (FLAIR) and T1-weighted pre- and post-gadolinium (Gd) spoiled gradient echo (SPGR) images. Diffusion-weighted images were acquired with a 6-directional axial diffusion-weighted echo-planar imaging (EPI) sequence with b = 1,000 s/mm^2 and 4 NEX, while DSC-PWI consisted of collecting a series of 80 T2*-weighted EPI images [TR/TE/flip = 1,500 ms/54 ms/35, 128 × 128 matrix, field of view (FOV) = 24 × 24 cm, 4 mm slice thickness] acquired before, during and after the bolus injection of 0.1 mmol/kg of body weight Gd-DTPA intravenously at the speed of 5 ml/s. Lactate-edited 3D point resolved spectroscopy (PRESS) ^{1}H-MRSI data were obtained using the parameters described by Park *et al.* (16), including a flyback echo-planar readout gradient in the superior–inferior (SI) dimension and an over-PRESS factor of 1.5 with very selective saturation (VSS) bands to avoid chemical shift artifacts (repetition time/echo time = 1,104/144 ms, FOV = 16 × 16 × 16 cm, voxel size = 1 × 1 × 1 cm, total acquisition time = 9.5 min, 712 dwell points and 988 Hz bandwidth). Anatomic images were used to define the PRESS region, which covered the lesion and 200–300 cc of normal tissue and avoided areas with sharply varying magnetic susceptibility and lipid contamination. Additional VSS bands were utilized to suppress residual lipid signals.

Within Exam Image Processing

All imaging and spectroscopic data were transferred offline to a Linux workstation. The FLAIR and pre-Gd T1-weighted images were rigidly aligned to the post-Gd T1-weighted images using previously developed software (22). Regions of interest (ROI) included normal-appearing white matter (NAWM), the contrast enhancing lesion (CEL), and the nonenhancing lesion (NEL), which was defined as the CEL subtracted from the T2-hyperintense lesion. CEL regions were manually defined on the co-registered post-Gd T1 SPGR images, excluding enhancement that was also present on the pre-Gd T1 images. The T2-hyperintense lesion was segmented based on the hyperintense signal on FLAIR images using a semiautomatic method (23). The resection cavity was excluded from all ROIs. NAWM was segmented automatically using a hidden Markov random field model with an expectation-maximization algorithm (24) on the pre-Gd T1 images.

ADC values were calculated on a voxel-by-voxel basis using software based on previously published algorithms (17), after alignment to the T2-weighted (b = 0) diffusion image to the T2-weighted FLAIR (25, 26). Perfusion datasets were nonrigidly aligned to the precontrast T1-weighted images using the VTK CISG software package (15) and rCBV, peak height and percentage recovery values were calculated for each voxel using software developed by our group. CBV was calculated by fitting the dynamic perfusion data by a modified gamma-variate function with a recirculation parameter, while peak height of the ΔR2* curve and percentage recovery were estimated nonparametrically. The spectroscopic data were processed using custom-designed software, described elsewhere (27), to generate maps of choline-to-NAA index (CNI) (28), a metric developed to describe the deviation of choline and NAA in regions of tumor relative to values in regions of normal brain tissue from the same individual. It is calculated using an iterative regression procedure, which eliminates

outliers that correspond to tumor by first estimating the ratio of Cho and NAA in “normal” brain from the slope of the line through the remaining voxels, and then defining the CNI for each voxel by its distance from the regression line divided by the standard deviation of the distance of normal voxels from the regression line. All spectroscopic voxels were visually inspected and manually excluded using SIVIC (29) if an unquantifiable low signal-to-noise ratio or artifacts were present. Only remaining voxels in the white matter were used for the analysis of normal-appearing voxels (NAV).

Inter-Exam Image Registration

The planning CT (pCT) was first rigidly aligned to the baseline precontrast T1-weighted image using FLIRT (26, 30), and the same transformation matrix was applied to the aligned dosimetry from MIM Vista (MIM Software, Cleveland, OH). Precontrast, T1-weighted images from the one- or two-month scan were used to correct for tissue shift around the tumor cavity through nonlinear registration [FNIRT (31)] to the baseline T1-weighted image. All images and associated ROIs from the progression scan were then rigidly aligned to the corrected T1-weighted intermediate image from the one- or two-month scan, providing a one-to-one mapping of voxels from the recurrence to the baseline scan. To mitigate errors due to alignment, all imaging, dosimetry data and CNI maps were resampled to 5 mm × 5 mm × 3 mm.

Voxel Classifications

Voxels were separated into three categories based on baseline anatomical imaging: 1. normal-appearing voxels (NAV; those that were outside of the CEL and NEL but within NAWM); 2. enhancing abnormal voxels (those within the CEL); and 3. nonenhancing abnormal voxels (those within the NEL). Histograms of each imaging parameter were plotted for each voxel category and for the subset of normal-appearing voxels at baseline that later progressed (defined as converting to either CEL or NEL tissue). Progressed voxels from NAV to NEL were grouped with those that progressed to CEL in this population because patients receiving anti-angiogenic therapy typically progress with a nonenhancing T2 lesion (21). For the latter, initial voxel categories were combined into four groups based on their category at both baseline and recurrence as shown in Fig. 2. Stable-NAV, or normal voxels, were defined as NAV voxels at both baseline and recurrence. Voxels that progressed consisted of those that progressed from either the NAV to NEL, NAV to CEL or NEL to CEL. Stable-nonenhancing (stable-NEL) voxels were defined as voxels in the NEL at baseline and recurrence, while stable-enhancing (stable-CEL) voxels were defined as voxels in the CEL at baseline and recurrence.

Data Analysis and Statistics

To determine whether a statistically significant difference existed among voxels in each voxel classification category, the median of each imaging parameter was computed for each category per patient as long as the classification region contained at least five voxels for that patient. For some categories, such as CNI within the CEL, this resulted in less than 24 patients available for analysis. Patient medians among groups were then compared using a Wilcoxon signed rank test. Within these groups, we further stratified for risk in both normal and progressing voxels by distance from the primary tumor. The distance of voxels that

progressed to the NEL were measured from the original T2 lesion boundary, and those that progressed to the CEL were measured from the edge of the CEL. Voxels were subdivided as either greater or less than 2 cm from the primary lesions based on the current definition for radiation treatment margins.

Predicting the Probability of Recurrence

To generate a model of the probability of recurrence, voxels were subdivided according to distance from the primary lesion and physiologic imaging parameters. Voxels were first subdivided by risk (with low and high risk being defined as 0–2 cm and 2–4 cm away from the primary lesion, respectively), and then binned by parameters found to be statistically significantly different among voxel classes, which included ADC, FA and CNI. Perfusion values did not reach the $P < 0.2$ cutoff for inclusion into the model. Voxels outside the respective PRESS box for a patient were not incorporated in the analysis that required both diffusion and spectroscopy. A distance cutoff of 4 cm from the primary lesion was used. ADC values were binned at 100-unit interval bins between 600 and 1,100, FA values at 0.05-unit increments between 0.2 and 0.55, and CNI at unit-intervals between 0–4. Voxel values outside of these ranges were assigned to the closest minimum or maximum bin values. The positive predictive value (PPV) was calculated as the percentage of voxels that recurred in each “bin”. To generate a predictive map for a particular patient, the values from the 23 other patients were used to generate the PPV matrix (leave-one-out cross-validation or LOOCV), then each voxel for the patient of interest was mapped to the appropriate PPV value by its distance (< or >2 cm), ADC, FA and CNI value.

Multinomial Model Integrating Dosimetry to Estimate the Likelihood of Voxel Progression

To integrate the effect of radiation on the likelihood of voxel progression, distance and dose were incorporated into a multinomial logistic regression model (MLRM). Univariate regression analysis was first performed for each variable and only parameters with $P < 0.05$ were used in the multivariate analyses. Consistent with our other analyses, perfusion parameters did not meet the required significance level to be analyzed in the multivariate model. A MLRM using the remaining variables was implemented using the R statistical software package, with the mlogit package [Eq. (1)], which enabled voxels from the same patient to be modeled as a random effect. Because the dose is planned according to distance from the tumor, we also included the interaction of dose and distance. Distance from the T1 and T2 lesions for each voxel was calculated as a continuous variable for this model. The likelihood of recurrence is expected to decrease as a function of increasing distance (1/min_dist) and with increasing dose (1/dose), and is reflected in the model.

Using LOOCV, individual voxel parameters of 23 training patients were combined according to Eq. (1), to provide a probability score per voxel based on the diffusion (ADC, FA), spectroscopy (CNI), distance from the edge of the baseline tumor volume and dose. The coefficients were determined by the best fit to the known results of each voxel within the 23 training patients, and the per-voxel PPV score was computed for the 24th patient by using the derived coefficients for each term in Eq. (1) (ADC, FA, CNI, distance and dose of each voxel) and solving the model equation for the 24th patient. To guard against overfitting, Akaike information criterion (AIC) was implemented in R software program, where the

optimal model was determined by repeated backwards-variable selection of the terms of the model until only a single model remained. The most accurate model was then selected and used to calculate the final predicted likelihood of recurrence per voxel for that patient.

This procedure was iteratively repeated for all patients, and the combined results were quantified using a receiver-operator-curve (ROC), and the area under the curve (AUC).

$$\begin{aligned}\text{group} \sim 1 \,|\, &\text{FA} + \text{ADC} + \text{CNI} + I\left(\frac{1}{\text{dose} \times \text{min\_dist}}\right) \\ &+ I\left(\frac{\text{CNI}}{\text{dose} \times \text{min\_dist}}\right) + I\left(\frac{\text{ADC}}{\text{dose} \times \text{min\_dist}}\right) \\ &+ I\left(\frac{\text{FA}}{\text{dose} \times \text{min\_dist}}\right).\end{aligned} \quad (1)$$

RESULTS

Patient Characteristics and Outcomes

Patient characteristics are shown in Table 1. The cohort of 15 males and 9 females had a median progression-free survival and overall survival of 10.8 (range: 1.7–29.7) and 18.4 (range: 8.7–59.2) months, respectively. Although no significant difference in overall survival was found between the two treatment groups, the subset of patients eligible for this study treated with enzastaurin did worse than those treated with bevacizumab and erlotinib [median overall survival 14.1 (95% CI; 9.8–29.3) vs. 20.6 (16.4–44.5) months; median progression-free survival 4.8 (1.9–9.6) vs. 12.6 (11–23) months].

Patterns of Recurrence

Voxel characteristics are shown in Table 2. A total of 117,418 white matter voxels in 24 patients were available for analysis, of which 107,430 were NAV at baseline, while 7,669 were in the NEL and 2,319 in the CEL. The voxels in each category per patient are listed in Supplementary Table S1 (http://dx.doi.org/10.1667/RR14662.1.S1). As expected, the majority of voxels (98,665) belonged to the stable-NAV group, representing either voxels with no subclinical involvement or voxels that were appropriately treated. The remaining NAV voxels at baseline were either NAV to NEL (8,022) or NAV to CEL (743). An additional 132 voxels in the NEL that progressed to the CEL were included in the progressed group. For voxels that were initially NAV at baseline, but part of the NEL and CEL at recurrence, the vast majority (90%) were nonenhancing, consistent with the known phenotype of nonenhancing recurrence in the setting of anti-angiogenic agents (32, 33). For the voxels that progressed into the NEL (N = 8,022), 77 and 95% recurred within 2 and 4 cm from the original T2 lesion, while 23% of voxels resided outside of the traditional 2-cm treatment boundary, highlighting the need for the identification of at-risk areas. Similarly, 20% of voxels recurring in the CEL were greater than 2 cm from the original CEL lesion, with 81 and 90% recurring within 2 and 4 cm, respectively. Figure 1 shows the patterns of recurrence as a function of distance (Fig. 1A and B) and dose (Fig. 1C and D) for voxels initially normal that progressed to the NEL and CEL. The vast majority of voxels within the

60 Gy isodose line progressed to the CEL, while those that progressed to the NEL had a more heterogeneous dose distribution.

Physiologic and Metabolic Characteristics of Voxels

Figure 2 shows the distribution of voxels for each imaging parameter as a function of their baseline and recurrence state. As expected, the voxels in NEL or CEL at baseline and recurrence had increased edema (Fig. 2A and D, panels i and ii, respectively), represented as a markedly elevated ADC and decreased FA when compared to normal voxels (panel iv). These effects were more pronounced in voxels within the CEL than the NEL, representing greater tumor burden. The CNI (Fig. 2C) was significantly elevated for voxels in the NEL and CEL compared to normal voxels, indicating more rapidly-dividing cells in these lesions. NAV voxels at baseline that progressed to NEL or CEL at recurrence had parameter values in between normal voxels and grossly pathologic voxels with elevated CNI and ADC and reduced FA, indicating subclinical involvement. Conversely, perfusion parameters were not significantly different for voxels that progressed compared to the stable-NAV group, as shown by the percentage recovery and rCBV values shown in Fig. 2B and E.

To more robustly identify parameters that are statistically significant for voxels that progress, histograms of parameter values were also analyzed per patient, as shown in Fig. 3 for NAV voxels progressing to CEL (left-side column) and NEL (center column) at recurrence, and compared to parameter values for stable, normal-appearing voxels (right-side column). For voxels that progressed to the NEL, statistically significant differences were observed for FA, ADC and CNI, with NAV voxels at baseline that exhibited decreased FA, increased ADC and increased CNI having a greater likelihood of progression. While voxels progressing into the NEL had no significant perfusion changes over stable-NAV, interestingly, voxels progressing into the CEL had a significantly lower percentage recovery from the perfusion data.

Discrete Model to Predict Recurrence

To predict the likelihood of a voxel progressing to the NEL or CEL from imaging parameters obtained at baseline, we constructed a model based on the statistically significant parameters (FA, ADC and CNI) identified by univariate regression analyses. A total of 21,140 voxels normal at baseline had both diffusion and spectroscopy data, of which 3,575 represented progressed voxels. Within the traditional 2-cm boundary, 9,329 voxels had diffusion and spectroscopy data, of which 2,920 progressed. Outside of the 2-cm boundary, 655 of the 11,811 voxels with both diffusion and spectroscopy data progressed.

Figure 4A and B shows the PPV of voxels between 0 and 2 cm, and >2 cm as a function of diffusion parameters and increasing CNI. CNI had a strong effect on the likelihood of progression both within and outside of the irradiated volume, even for voxels with normal diffusion parameters. The PPV grew with increasingly abnormal diffusion parameters, with elevated CNI potentiating the effect. For voxels >2 cm from the boundary of the standard radiation field with normal physiologic and metabolic parameters, the likelihood of progression was almost zero, while in voxels with elevated CNI, those with abnormal diffusion parameters exhibited a higher PPV. Voxels with a CNI value greater than 4 were

likely to progress regardless of diffusion value. When using a model for the likelihood of progression that only utilized diffusion and spectroscopy (not distance), an AUC of 0.68 was achieved. Incorporating distance as a binary category (≤2 or >2 cm) increased the AUC to 0.75.

Continuous Model to Predict Recurrence

The model described by Eq. (1), all terms were significant in all iterations, except for "*FA/(dose × min_dist)*" in 5 of the 24 patients (see Fig. 4C for results of the model). The likelihood of progression is shown on the Y-axis as a function of varying a single parameter on the X-axis for each NAV, at distance of both 1 and 3 cm from the initial tumor. The remaining baseline parameters were set at the median values of the normal voxels (ADC = 806, FA = 0.42, CNI = 0.10, dose = 33 Gy) so the effect of varying a single parameter could be visualized. The likelihood of progression increased with elevated ADC, decreased FA and increased CNI, with both increasing distance and dose significantly decreasing the likelihood of progression. Notably, an incremental increase in dose had the greatest effect in the low-dose region (<45 Gy), with diminishing benefit on the likelihood of recurrence for higher doses. The results of the ROC analysis yielded an AUC of 0.76.

To illustrate the utility of the model in treatment planning, we applied it to create PPV maps for the three examples shown in Fig. 5. Figure 5A represents an example where the increased likelihood of recurrence predicted by the model extends across the white matter tracks of the corpus callosum to the contralateral hemisphere corresponding to the T2-hyperintensity lesion at recurrence, and reflects the effects of increased CNI and decreased FA despite being located within the high-dose region. Figure 5B shows a representative case where the likelihood of recurrence corresponds to the area of elevated CNI at baseline and dose <60 Gy, and correctly identifies the new T2 lesion at recurrence. Figure 5C shows the ability of the model to predict a distant recurrence in the low-dose region where spectroscopy was not available. In this example, the model predicted recurrence based on diffusion, dose and distance parameters only, whereby the region of low dose drove an increased risk of recurrence in the contralateral frontal lobe that corresponded to the new T2 lesion at recurrence.

DISCUSSION

Radiotherapy is an essential component of treatment for high-grade gliomas, providing a proven overall survival benefit. Despite increases in dose and variation in the radiation volume, recurrences remain largely local and controversy remains over the correct definition and dose of at-risk voxels, as demonstrated in the differing criteria of two large cooperative groups [RTOG and EORTC (34)]. Notwithstanding advances in modern imaging, radiotherapy is primarily guided by anatomic T1 and T2 sequences, with guidelines suggesting a purely geometric expansion, bounded by anatomic barriers. This geometric expansion often leads to irradiation of normal brain tissue, affecting cognitive sequela (35) and quality of life (36), while underdosing at-risk voxels outside the traditional 2-cm boundary. While our results showed that the majority of voxels recurred within 2 cm of the primary tumor T2 lesion boundary, which is consistent with previously reported studies, we

found that 25% of voxels recurred outside this margin. This illustrates the importance of identifying at-risk voxels outside of the traditional irradiated margin. We also found that 75% of voxels within the 2-cm margin did not progress, representing either appropriately or over-treated voxels with no significant subclinical involvement. With the advent of novel systemic agents that can potentiate the effect of radiotherapy, it has become crucial to correctly identify voxels at risk for progression to accurately target radiation.

Despite advances in modern imaging and radiation delivery, current treatment strategies do not integrate physiologic and metabolic imaging to guide dose and spatial distribution in radiotherapy. Incorporating multi-modal imaging can potentially enable voxel-level, risk-adapted radiation treatment by identifying voxels with subclinical disease that have a high likelihood of recurrence outside of the traditional high-risk area. In addition, this approach may help to determine which voxels within the traditional radiation margins have a low chance of recurrence. The creation of a voxel-level predictive map, based on quantitative imaging parameters and dose to each voxel developed in this study, can enable future risk-adapted radiotherapy, potentially increasing local control while mitigating toxicity. To our knowledge, this is the first effort to model an individual voxel's likelihood of recurrence before treatment to provide a framework for future risk-adapted radiation treatment planning.

Although other studies have analyzed the effect of physiologic characteristics within the tumor itself (37, 38), we have demonstrated how abnormal baseline physiologic and metabolic imaging metrics in otherwise anatomically normal-appearing tissue can be used along with planned dosimetry information to predict a voxel's likelihood of future recurrence. Our results confirmed the hypothesis that voxels at risk for progression would harbor subclinical disease and therefore have physiologic and metabolic parameters, which were in between voxels, that were completely normal and grossly pathologic by indicating that the combination of ADC, FA and CNI can identify normal-appearing voxels at baseline likely to progress at recurrence. The amount of cell turnover, as indicated by elevated CNI, had the greatest effect of a voxel's likelihood of progression, significantly potentiating the effect of abnormal diffusion parameters.

The observed elevation of the ADC in NAV at baseline that was associated with an increased likelihood of recurrence suggests that measured ADC values were dominated by the presence of subclinical edema caused by microscopic disease infiltration. Our results also showed that increased dose decreased the likelihood of progression, but had diminishing benefits with higher doses, consistent with the failure of dose-escalation studies above 60 Gy. For voxels recurring in the nonenhancing lesion, no effect of perfusion parameters on the likelihood of progression was seen. These findings are consistent with the notion that subclinical disease involves small populations of infiltrative cells that have not yet formed neovasculature, or could be due to the vascular normalization that results from anti-angiogenic therapy. However, for the small subset of normal voxels that progressed to the CEL at recurrence, the amount of vessel leakiness (represented by reduced percentage recovery) was significantly elevated in these voxels, indicating that neovasculature had already begun to form.

The prediction of disease recurrence was made more challenging by treatment with agents that have anti-angiogenic properties and result in a more diffuse and infiltrative recurrence pattern (39). In this study, the vast majority of voxels that progressed became nonenhancing tumor, consistent with the use of an anti-angiogenic agent. The predominance of voxels recurring in the NEL, the associated lack of perfusion abnormalities, and the elevated rather than reduced ADC in NAV at baseline being associated with an increased likelihood of recurrence, were likely the result of the concomitant anti-angiogenic therapy our cohort received. Because our findings were based on a population that used an upfront anti-angiogenic agent [a strategy explored in recent clinical trials (9, 10)], the model generated may not be directly applicable to patients undergoing standard therapy (5) for glioblastoma. Nonetheless, the methodology and model developed here can be easily trained on and applied to other cohorts of irradiated patients treated with different adjuvant therapies. Although two agents with different mechanisms of action and potentially distinct patterns of recurrence were utilized, the baseline images used to predict recurrent voxels were obtained before the administration of all therapy and were free of the effects of the treatments.

Despite the potential impact of our results on radiotherapy planning, there are several methodological limitations to this study. The accuracy of the model is mostly limited by the fact that not all voxels are equally represented across the entire range of parameters (for example, spectroscopy data was not routinely obtained for voxels far from the tumor) and the fact that guidelines for radiotherapy planning are relatively standardized. The latter results in a somewhat homogeneous dose distribution across patients (for example, 60 Gy to the CEL and 45–60 Gy to the NEL) with lower doses to voxels far from the tumor. This in turn may limit the reliability of the model in areas not well represented within the data set, such as high-dose voxels far from the tumor or low-dose voxels close to the tumor. While this limitation is most pronounced in the discrete model, the MLRM model still enables us to derive trends based on the existing data. Future prospective studies that accrue additional patients would add increasing diversity to the dataset, which could improve the ability to identify voxels likely to progress, and could take advantage of the improved MRSI acquisition schemes that include automatic prescription with larger fields of view that have since become routine in serial studies. In addition, methods to achieve higher resolution MRSI data should also be considered for this application. A final source of error inherent to such voxel-level serial analyses originates from aligning images from two different time points and is exacerbated by tissue shift around the tumor cavity. However, we minimized error due to registration by resampling all images to a lower (5 × 5 mm) resolution and using the two-month scan as an intermediate image in the alignment to accommodate shifting morphology after surgery.

In conclusion, in these data, we have shown that voxels outside of the contrast enhancing and T2 lesions that are likely to recur have a significantly different physiologic and metabolic signature than voxels that do not progress. Using a model that combines dosimetry, distance and quantitative metrics obtained from physiologic and metabolic MRI, we were able to both generate maps that are predictive of the likelihood of progression, and model the decreased likelihood of progression with increasing dose. The framework provided can be applied in future studies of larger cohorts of patients to evaluate the

potential of voxel-level, risk-adapted radiotherapy planning strategies in improving survival and quality of life.

Supplementary Material

Refer to Web version on PubMed Central for supplementary material.

Acknowledgments

This work was supported by the National Institutes of Health, grant nos. R01 CA127612 and P01 CA118816.

References

1. Wen PY, Kesari S. Malignant gliomas in adults. N Engl J Med. 2008; 359:492–507. [PubMed: 18669428]
2. Giese A, Bjerkvig R, Berens ME, Westphal M. Cost of migration: invasion of malignant gliomas and implications for treatment. J Clin Oncol. 2003; 21:1624–36. [PubMed: 12697889]
3. Simpson JR, Horton J, Scott C, Curran WJ, Rubin P, Fischbach J, et al. Influence of location and extent of surgical resection on survival of patients with glioblastoma multiforme: results of three consecutive radiation therapy oncology group (RTOG) clinical trials. Int J Radiat Oncol Biol Phys. 1993; 26:239–44. [PubMed: 8387988]
4. Stummer W, Reulen H-J, Meinel T, Pichlmeier U, Schumacher W, Tonn J-C, et al. Extent of resection and survival in glioblastoma multiforme: identification of and adjustment for bias. Neurosurgery. 2008; 62:564–76. [PubMed: 18425006]
5. Stupp R, Mason WP, Van Den Bent MJ, Weller M, Fisher B, Taphoorn MJ, et al. Radiotherapy plus concomitant and adjuvant temozolomide for glioblastoma. N Engl J Med. 2005; 352:987–96. [PubMed: 15758009]
6. Shapiro WR, Green SB, Burger PC, Mahaley MS Jr, Selker RG, VanGilder JC, et al. Randomized trial of three chemotherapy regimens and two radiotherapy regimens in postoperative treatment of malignant glioma. J Neurosurg. 1989; 71:1–9.
7. Hochberg FH, Pruitt A. Assumptions in the radiotherapy of glioblastoma. Neurology. 1980; 30:907–11. [PubMed: 6252514]
8. Gaspar LE, Fisher BJ, Macdonald DR, Leber DV, Halperin EC, Schold SC Jr, et al. Supratentorial malignant glioma: patterns of recurrence and implications for external beam local treatment. Int J Radiat Oncol Biol Phys. 1992; 24:55–7. [PubMed: 1512163]
9. Chinot OL, Wick W, Mason W, Henriksson R, Saran F, Nishikawa R, et al. Bevacizumab plus radiotherapy-temozolomide for newly diagnosed glioblastoma. N Engl J Med. 2014; 370:709–22. [PubMed: 24552318]
10. Cloughsey T, Wick W, Mason W, Henriksson R, Saran F, Nishikawa R, et al. Phase III trial of bevacizumab added to standard radiotherapy and temozolomide for newly diagnosed glioblastoma: final progression-free survival and preliminary overall survival results from avaglio (PL02.002). Neurology. 2013; 80:PL02.002.
11. Friedman HS, Prados MD, Wen PY, Mikkelsen T, Schiff D, Abrey LE, et al. Bevacizumab alone and in combination with irinotecan in recurrent glioblastoma. J Clin Oncol. 2009; 27:4733–40. [PubMed: 19720927]
12. de Groot JF, Fuller G, Kumar AJ, Piao Y, Eterovic K, Ji Y, et al. Tumor invasion after treatment of glioblastoma with bevacizumab: radiographic and pathologic correlation in humans and mice. Neuro Oncol. 2010; 12:233–42. [PubMed: 20167811]
13. Nelson SJ. Assessment of therapeutic response and treatment planning for brain tumors using metabolic and physiological MRI. NMR Biomed. 2011; 24:734–49. [PubMed: 21538632]
14. Nelson SJ, Cha S. Imaging glioblastoma multiforme. Cancer J. 2003; 9:134–45. [PubMed: 12784879]

15. Pirzkall A, McKnight TR, Graves EE, Carol MP, Sneed PK, Wara WW, et al. MR-spectroscopy guided target delineation for high-grade gliomas. Int J Radiat Oncol Biol Phys. 2001; 50:915–28. [PubMed: 11429219]
16. Park I, Tamai G, Lee MC, Chuang CF, Chang SM, Berger MS, et al. Patterns of recurrence analysis in newly diagnosed glioblastoma multiforme after three-dimensional conformal radiation therapy with respect to pre-radiation therapy magnetic resonance spectroscopic findings. Int J Radiat Oncol Biol Phys. 2007; 69:381–9. [PubMed: 17513061]
17. Pirzkall A, Li X, Oh J, Chang S, Berger MS, Larson DA, et al. 3D MRSI for resected high-grade gliomas before RT: tumor extent according to metabolic activity in relation to MRI. Int J Radiat Oncol Biol Phys. 2004; 59:126–37. [PubMed: 15093908]
18. Chuang CF, Chan AA, Larson D, Verhey LJ, McDermott M, Nelson SJ, et al. Potential value of MR spectroscopic imaging for the radiosurgical management of patients with recurrent high-grade gliomas. Technol Cancer Res Treat. 2007; 6:375–82. [PubMed: 17877425]
19. Butowski N, Chang SM, Lamborn KR, Polley MY, Parvataneni R, Hristova-Kazmierski M, et al. Enzastaurin plus temozolomide with radiation therapy in glioblastoma multiforme: A phase I study. Neuro Oncol. 2010; 12:608–13. [PubMed: 20156802]
20. Butowski N, Chang SM, Lamborn KR, Polley MY, Pieper R, Costello JF, et al. Phase II and pharmacogenomics study of enzastaurin plus temozolomide during and following radiation therapy in patients with newly diagnosed glioblastoma multiforme and gliosarcoma. Neuro Oncol. 2011; 13:1331–8. [PubMed: 21896554]
21. Wen PY, Macdonald DR, Reardon DA, Cloughesy TF, Sorensen AG, Galanis E, et al. Updated response assessment criteria for high-grade gliomas: response assessment in neuro-oncology working group. J Clin Oncol. 2010; 28:1963–72. [PubMed: 20231676]
22. Nelson SJ, Nalbandian AB, Proctor E, Vigneron DB. Registration of images from sequential MR studies of the brain. J Magn Reson Imaging. 1994; 4:877–83. [PubMed: 7865950]
23. Saraswathy, S., Crawford, F., Nelson, SJ. Semi-automated segmentation of brain tumor lesions in MR images; Proc Intl Soc Mag Reson Med. 2006. p. 14http://bit.ly/2s9e2or
24. Zhang Y, Brady M, Smith S. Segmentation of brain MR images through a hidden Markov random field model and the expectation-maximization algorithm. IEEE Trans Med Imaging. 2001; 20:45–57. [PubMed: 11293691]
25. Nelson SJ, Nalbandian AB, Proctor E, Vigneron DB. Registration of images from sequential MR studies of the brain. J Magn Reson Imaging. 2005; 4:877–83.
26. Fischer, B., Modersitzki, J. FLIRT: A flexible image registration toolbox. In: Gee, J.Maintz, JBA., Vannier, M., editors. Biomedical image registration. Lecture notes in computer science. Vol. 2717. Berlin Heidelberg: Springer; 2003. p. 261-70.
27. McKnight TR, von dem Bussche MH, Vigneron DB, Lu Y, Berger MS, McDermott MW, et al. Histopathological validation of a three-dimensional magnetic resonance spectroscopy index as a predictor of tumor presence. J Neurosurg. 2002; 97:794–802. [PubMed: 12405365]
28. McKnight TR, Noworolski SM, Vigneron DB, rer Nat ND, Sarah J. An automated technique for the quantitative assessment of 3D–MRSI data from patients with glioma. J Magn Reson Imaging. 2001; 13:167–77. [PubMed: 11169821]
29. Crane JC, Olson MP, Nelson SJ. SIVIC: open-source, standards-based software for DICOM MR spectroscopy workflows. J Biomed Imaging. 2013; 2013:12.
30. Jenkinson M, Bannister P, Brady M, Smith S. Improved optimization for the robust and accurate linear registration and motion correction of brain images. Neuroimage. 2002; 17:825–41. [PubMed: 12377157]
31. Andersson, JL., Jenkinson, M., Smith, S. FMRIB Technical Report TR07JA2. Oxford: FMRIB Centre; 2007. Non-linear registration, aka spatial normalisation. http://bit.ly/2s9fUgZ
32. Iwamoto FM, Abrey LE, Beal K, Gutin PH, Rosenblum MK, Reuter VE, et al. Patterns of relapse and prognosis after bevacizumab failure in recurrent glioblastoma. Neurology. 2009; 73:1200–6. [PubMed: 19822869]
33. Spalding AC, Wagner SA, Vitaz TW. Concurrent bevacizumab and temozolomide alters the pattern of failure in radiation treatment of glioblastoma multiforme. Int J Radiat Oncol Biol Phys. 2010; 78:S10.

34. Fogh S, Wahl M, Anwar M, Haas-Kogan D, Clarke JL, Sneed PK. Standardization and quality assurance of radiation therapy volumes for adults with high-grade gliomas. Semin Radiat Oncol. 2014; 24:259–64. [PubMed: 25219810]

35. Archibald YM, Lunn D, Ruttan LA, Macdonald DR, Del Maestro RF, Barr HWK, et al. Cognitive functioning in long-term survivors of high-grade glioma. J Neurosurg. 1994; 80:247–53. [PubMed: 8283263]

36. Cheng J-X, Zhang X, Liu B-L. Health-related quality of life in patients with high-grade glioma. Neuro Oncol. 2009; 11:41–50. [PubMed: 18628405]

37. Oh J, Henry RG, Pirzkall A, Lu Y, Li X, Catalaa I, et al. Survival analysis in patients with glioblastoma multiforme: Predictive value of choline-to-n-acetylaspartate index, apparent diffusion coefficient, and relative cerebral blood volume. J Magn Reson Imaging. 2004; 19:546–54. [PubMed: 15112303]

38. Crawford F, Khayal I, McGue C, Saraswathy S, Pirzkall A, Cha S, et al. Relationship of pre-surgery metabolic and physiological MR imaging parameters to survival for patients with untreated GBM. J Neurooncol. 2009; 91:337–51. [PubMed: 19009235]

39. Narayana A, Kunnakkat SD, Medabalmi P, Golfinos J, Parker E, Knopp E, et al. Change in pattern of relapse after antiangiogenic therapy in high-grade glioma. Int J Radiat Oncol Biol Phys. 2012; 82:77–82. [PubMed: 21163583]

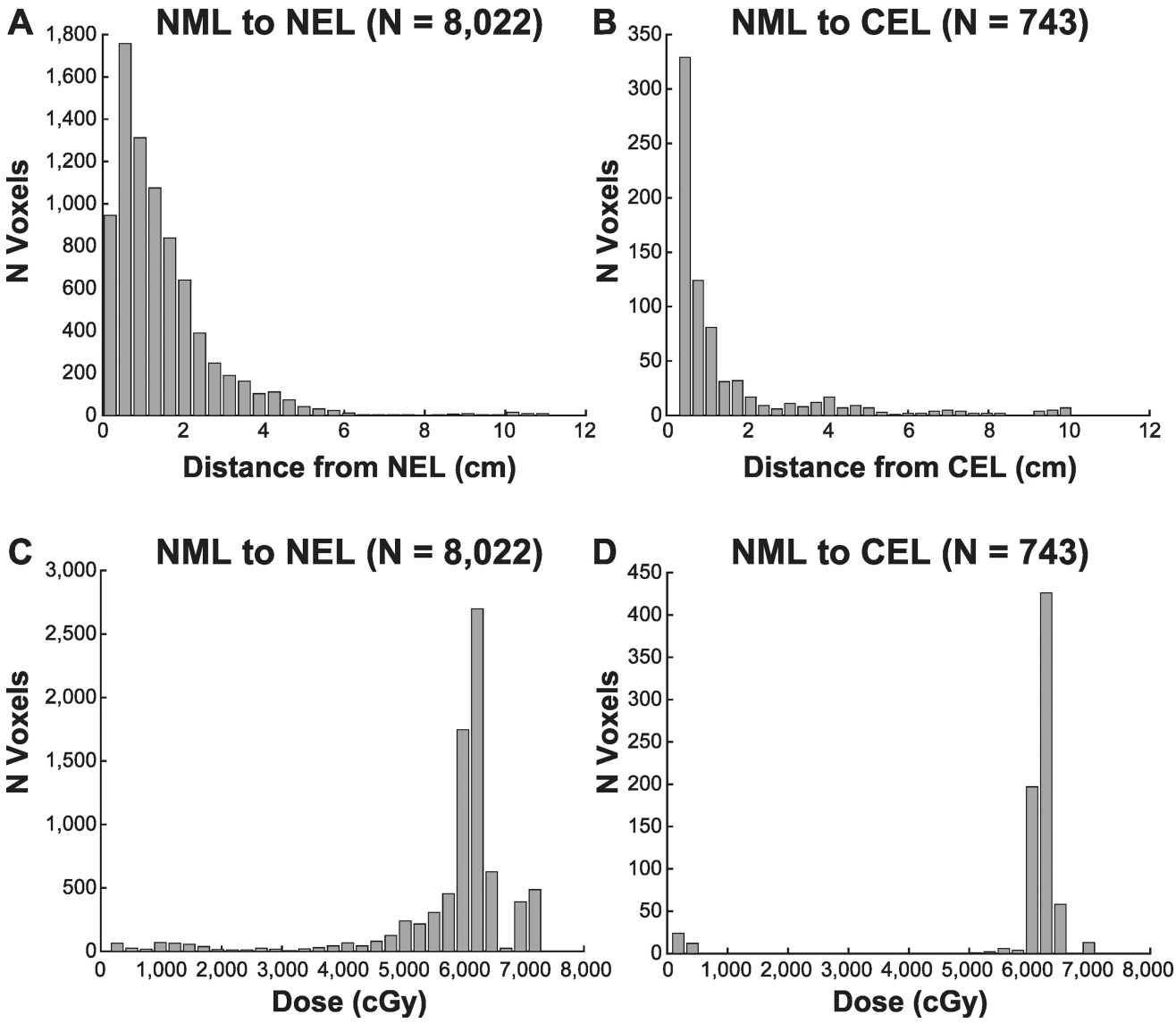

FIG 1.

Patterns of recurrence. Panels A and B: Distribution of normal appearing voxels (NAV) that progressed to the NEL or CEL versus the distance from the initial nonenhancing or enhancing tumor. Panels C and D: Distribution of progressing voxels as a function of radiation dose.

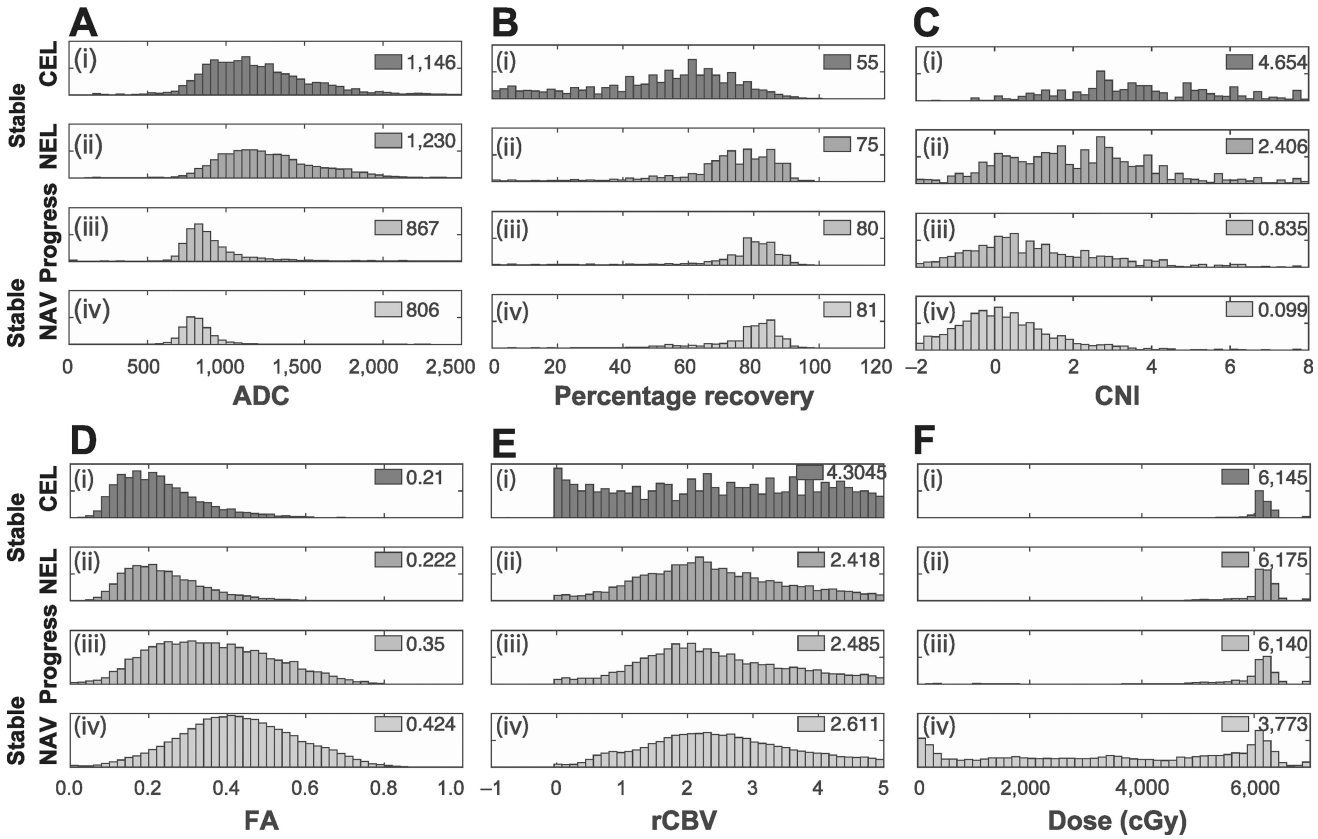

FIG 2.

The distribution of voxel parameters value by voxel type and parameter, with stable enhancing [stable-CEL (panel i)] and nonenhancing [stable-NEL (panel ii)] tumor, compared with NAV voxels that progress (panel iii) and those that remain uninvolved [stable-NAV (panel iv)]. Voxels from all patients were concatenated into a single dataset. Median values are shown for each parameter and voxel type. Panel A: Apparent diffusion coefficient; panel B: percentage recovery; panel C: choline to NAA index; panel D: fractional anisotropy; panel E: relative cerebral blood volume; and panel F: radiation dose.

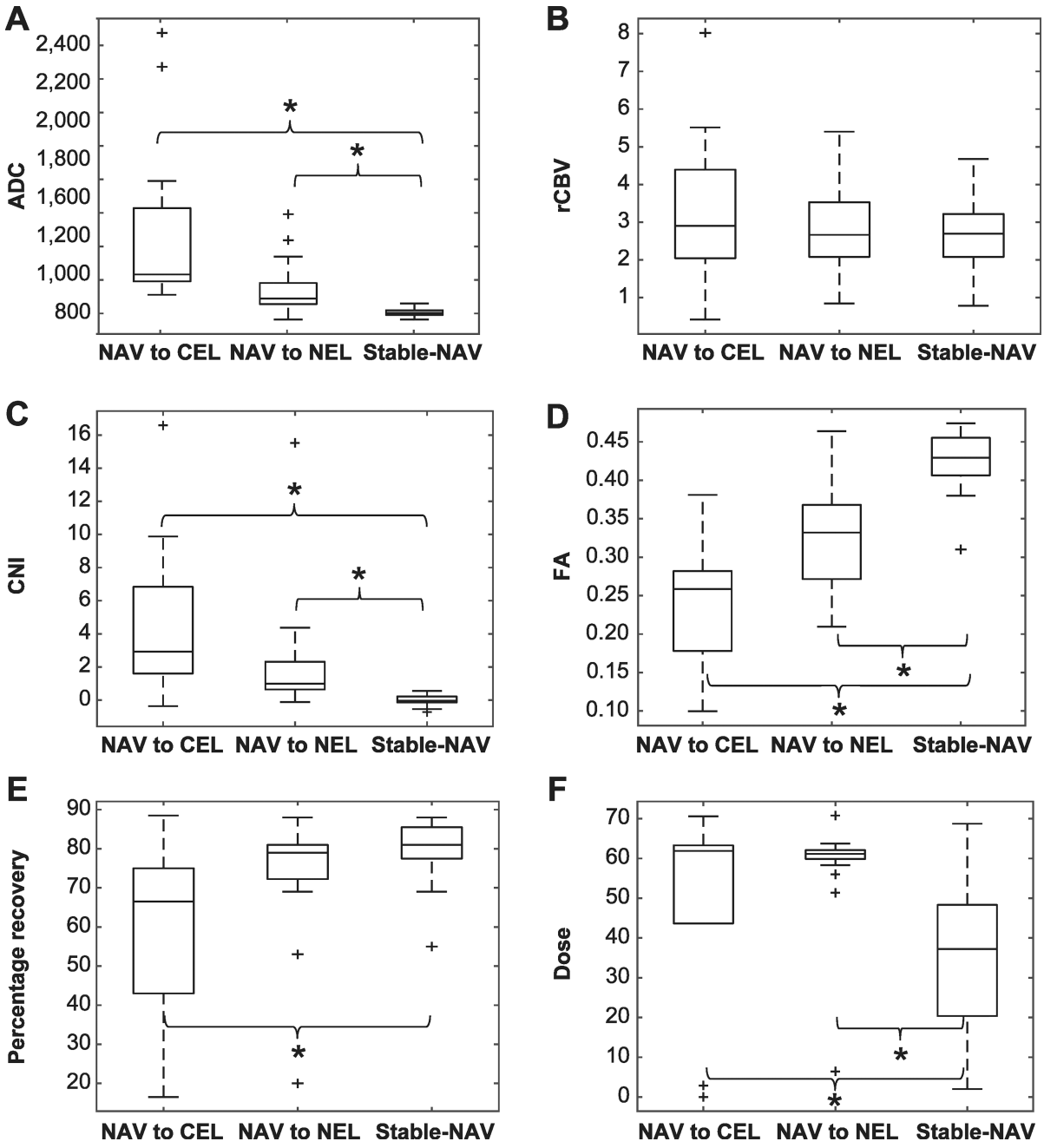

FIG 3.

Box plots of the median value of each patient's voxels, by parameter, that progress from the NAV at baseline to the CEL and NEL, and remain as stable NAV, respectively, at recurrence. Panel A: Apparent diffusion coefficient; panel B: percentage recovery; panel C: choline to NAA index; panel D: fractional anisotropy; panel E: relative cerebral blood volume; and panel F: radiation dose.

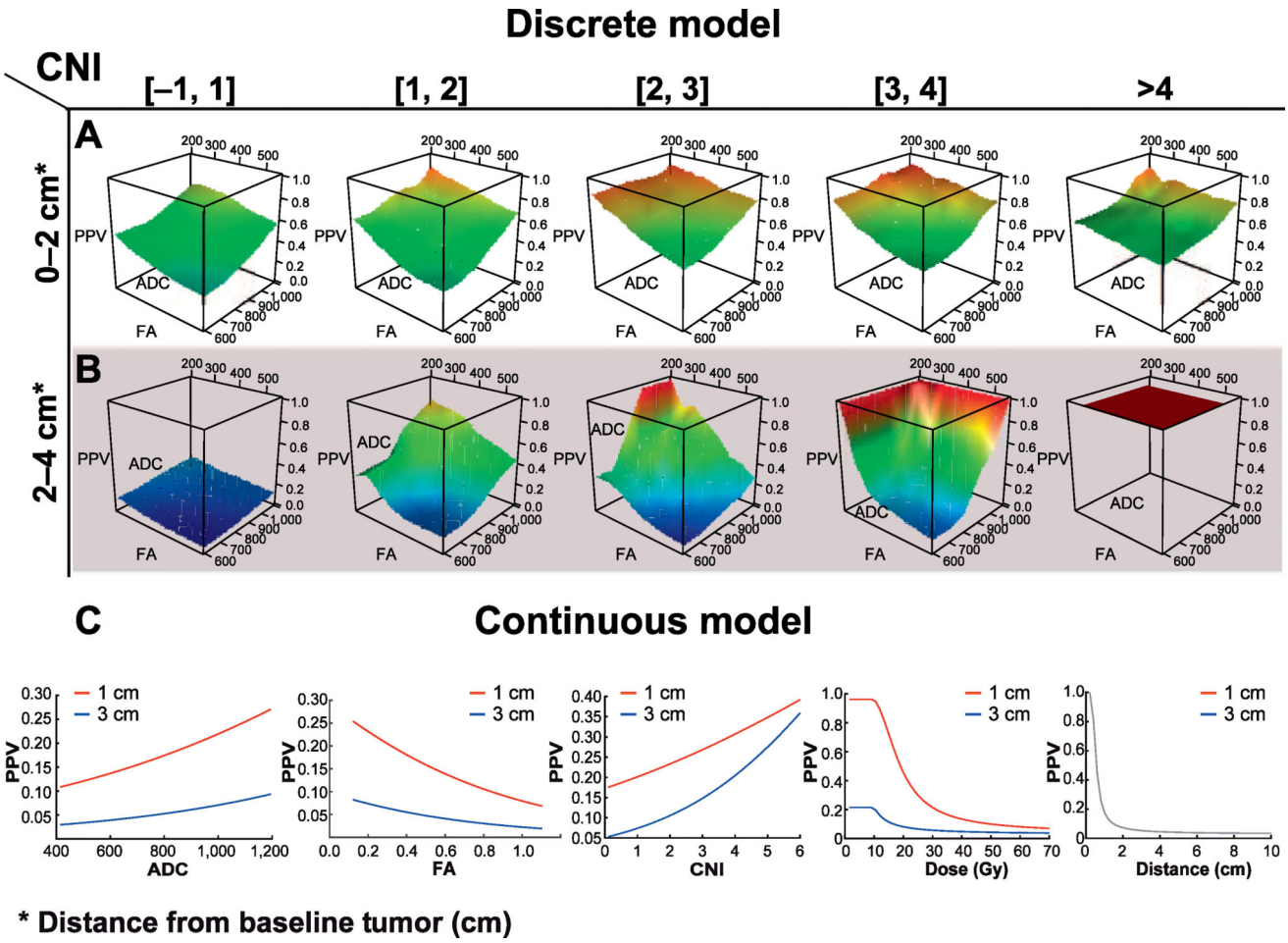

FIG 4.

Likelihood of progression [positive predictive value (PPV)] of voxels NAV at baseline progressing into the NEL or CEL at recurrence, as function of voxel parameters. Panels A and B demonstrate the PPV of voxels using the discrete model, whereby voxels are subdivided by their distance from the primary tumor (panel A: 0–2 cm; and panel B: 2–4 cm) and their CNI values (top). Within each group of voxels with similar CNI values and distance from the primary tumor, the PPV is calculated for voxels as a function of ADC and FA. Panel C shows the results of the continuous model [Eq. (1)], whereby the effect of a single parameter on the PPV is illustrated by sweeping through a range of values while holding all other parameters constant. This is done for a voxel at 1 and 3 cm, illustrating the strong effect of distance on likelihood of recurrence.

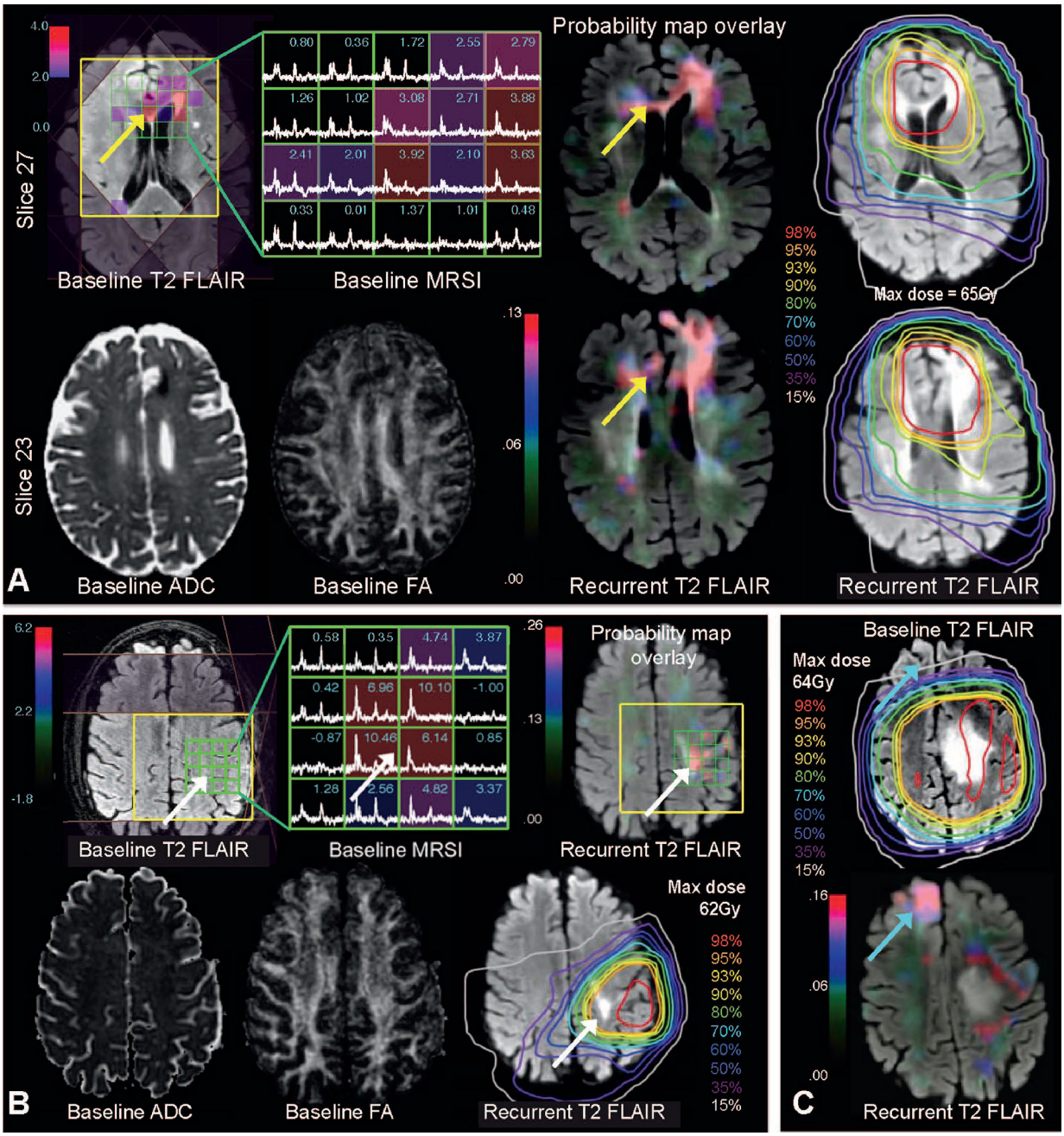

FIG 5.

Panel A: Baseline T2 and FA (left side, bottom) showing tumor in the left frontal lobe (abutting the falx cerebri) with corresponding T2 hyperintensity and disruption in white matter tracts. Spectroscopy from the same baseline scan is overlaid on FLAIR MRI (left side, top) showing increased CNI extending to the contralateral lobe. The likelihood of recurrence predicted from the model is mapped onto the recurrent FLAIR image on the two different slices with the corresponding dosimetry (right side), correctly predicting recurrence along the genu of the corpus callosum (yellow arrows). Panel B: Another example in a different patient showing a local recurrence predicted in the high-dose area. The baseline

FLAIR, ADC and FA are shown, and the map of likelihood of recurrence (i.e., probability map) highlights an area just superior to the initial tumor with elevated CNI (white arrows). This corresponds to the area of recurrence seen on FLAIR, despite being in the high dose region. Panel C: A third example showing recurrence far from the original tumor. The top slice shows the baseline tumor on FLAIR overlaid with a large radiation field. The bottom slice shows the recurrent FLAIR image overlaid with the probability map, correctly showing recurrence at the contralateral frontal lobe, in a low-dose region (blue arrows).

TABLE 1

Patient Characteristics

Trial	All	Bevacizumab	Enzastaurin
N	24	13	11
Age (years)	52	51	57
Progression-free survival (days)	323	377	142
Overall survival (days)	552	619	422
Male	15	6	9
Female	9	7	2
GTR	11	7	4
STR	11	5	6
Biopsy	2	1	1

TABLE 2

Voxel Characteristics

Baseline		Recurrence	Category	N	Median				
					Fractional anisotropy	Apparent diffusion coefficient	Percentage recovery	Relative cerebral blood volume	Choline-to-NAA index
NAV	→	NAV	Normal	98,665	0.43	804	81	2.6	0.05
NAV	→	NEL	Worse	8,022	0.36	860	80	2.4	0.67
NAV	→	CEL	Worse	743	0.28	1,014	70	4.2	2.67
NEL	→	NEL	Stable	2,742	0.22	1,233	73	2.4	2.42
NEL	→	CEL	Worse	132	0.21	1,142	65	3.6	3.0
CEL	→	CEL	Stable	263	0.23	1,078	44	3.8	6.6